Stable Triphenolamine Radical Cathode with High Electron Conductivity for High-Rate Aqueous Zinc-ion Batteries

*Jiaxing Huang,[a] Meilin Li,[b] Cuiping Han,[*b] and Yuan Li[*a]*

a. J. Huang, Prof. Y. Li
Institute of Polymer Optoelectronic Materials and Devices,
State Key Laboratory of Luminescent Materials and Devices,
South China University of Technology,
Guangzhou, 510640 (P. R. China)
E-mail: celiy@scut.edu.cn

b. M. Li, Prof. C. Han
Faculty of Materials Science and Energy Engineering
Shenzhen University of Advanced Technology
Shenzhen 518055, (P. R. China)
E-mail: cp.han@siat.ac.cn

Keywords: open-shell radicals, N-heteroaromatic materials, organic cathodes, aqueous Zn-ion batteries, Zn-organic batteries.

Abstract: Comparing with conventional lithium-ion batteries with organic electrolyte, aqueous zinc-ion batteries with low cost, sustainable and environment-friendly organic cathodes exhibit promising potential to meet the continuously increasing demand on safe and large-scale energy storage. The representative organic cathodes, including quinoidal polycyclic aromatic hydrocarbons (PAHs) and 2,2,6,6-tetramethylpiperidinyl-N-oxyl (TEMPO) polymers, suffer from the challenging synthesis and limited theoretical specific capacity. Herein, different from PAHs and TEMPO polymers, a stable 4,4',4"-nitrilotriphenol (TPA-$(OH)_3$) is explored as organic radical cathode material by extremely low-cost raw materials and two simple reactions. Furtherly, an open-shell TPA-O_3 radical is obtained by a facile oxidation with air. Interestingly, TPA-O_3 showed unexpected higher electron conductivity of 3.35×10^{-4} S cm^{-1} than the precursor (2.73×10^{-6} S cm^{-1} for TPA-$(OMe)_3$). The nitro-like nitroxide resonance structures of TPA-O_3 contribute to its high electrochemical stability during the 200-cycle cyclic voltammetry test in air and thus exhibits good reversibility when used as a cathode material. Moreover, TPA-O_3 exhibit high reduction voltage of 1.02~1.33 V vs, Zn/Zn^{2+}, stable capacities of 123.7 mAh g^{-1} and high-capacity retention of 95.87% after 2000 stable cycles at 5 A g^{-1}, which is superior to previously reported organic radical cathodes.

1. Introduction

Over the past few decades, developments in lithium-ion battery have accelerated the power supply for portable electronic devices and electric vehicles.[1] However, the rapid growth in demand for lithium-ion batteries has led to global lithium resource scarcity and rising costs, which have caused environmental challenges and issues related to battery recycling and disposal.[2] Aqueous zinc-ion batteries (ZIBs) have attracted extensive attention and development due to their abundant zinc resources, high theoretical specific capacity of Zn (up to 820 mAh g^{-1}), and non-flammability of aqueous electrolyte.[3] To date, the researches based on cathode materials for ZIBs mainly focus on manganese-based oxides (e.g. MnO_2),[4] vanadium-based oxides (e.g. VO_2, V_2O_5),[5] prussian blue analogues,[6] and organic compounds.[7] For these inorganic cathodes, the strong electrostatic interaction caused by the divalent Zn^{2+} with high charge density, and the volume change arose from large-sized hydrated Zn^{2+} easily lead to severe structural collapse of inorganic compounds.[8] Moreover, there are obvious problems in ZIBs constructed of inorganic cathodes, such as slow Zn^{2+} transport kinetics,[9] capacity fading,[10] and dissolution of the electrode components,[11] which do not meet the environmental requirements of green and sustainable development.

Organic materials with advantages of tuneable chemical structures, intrinsic flexibility and low cost have received widespread attention in various fields such as photovoltaic, photothermal materials, and energy storage batteries.[12] Recently, organic materials are considered as promising candidates for energy storage battery electrodes due to their structural diversity, renewability, and environmental friendliness.[7c,13] Among them, organic open-shell radicals with one or more unpaired electrons exhibit unique characteristics (e.g. high redox potential, fast electron-transfer rate and good electrochemical reversibility[14]), which are difficult to achieve in closed-shell molecules.[12l,12m] Nonetheless, radicals are generally sub-valent compounds that can readily undergo self-polymerization, hydrogen abstraction, or coupling to satisfy valency, which can subject them to high intrinsic thermodynamic and kinetic reactivity,[15] and also the short lifetimes due to their instability.[16] Therefore, it is urgent to prepare organic radicals with high photothermal and electrochemical stability in air.[17]

On one hand, one of the classic strategies to stabilize radicals is introduction of large steric hindrance groups, such as triphenylmethyl or tris(2,4,6-trichlorophenyl)methyl radical, to avoid the reaction of radical with active species (e.g. oxygen and water).[18] The phenyl rings and chlorine atoms of these radical reduce the contact of the reactive radical site with external active species, thereby efficiently improving the chemical and thermal stability. Another typical stable radical with the steric protection of four methyl groups is 2,2,6,6-tetramethylpiperidinyl-N-oxyl

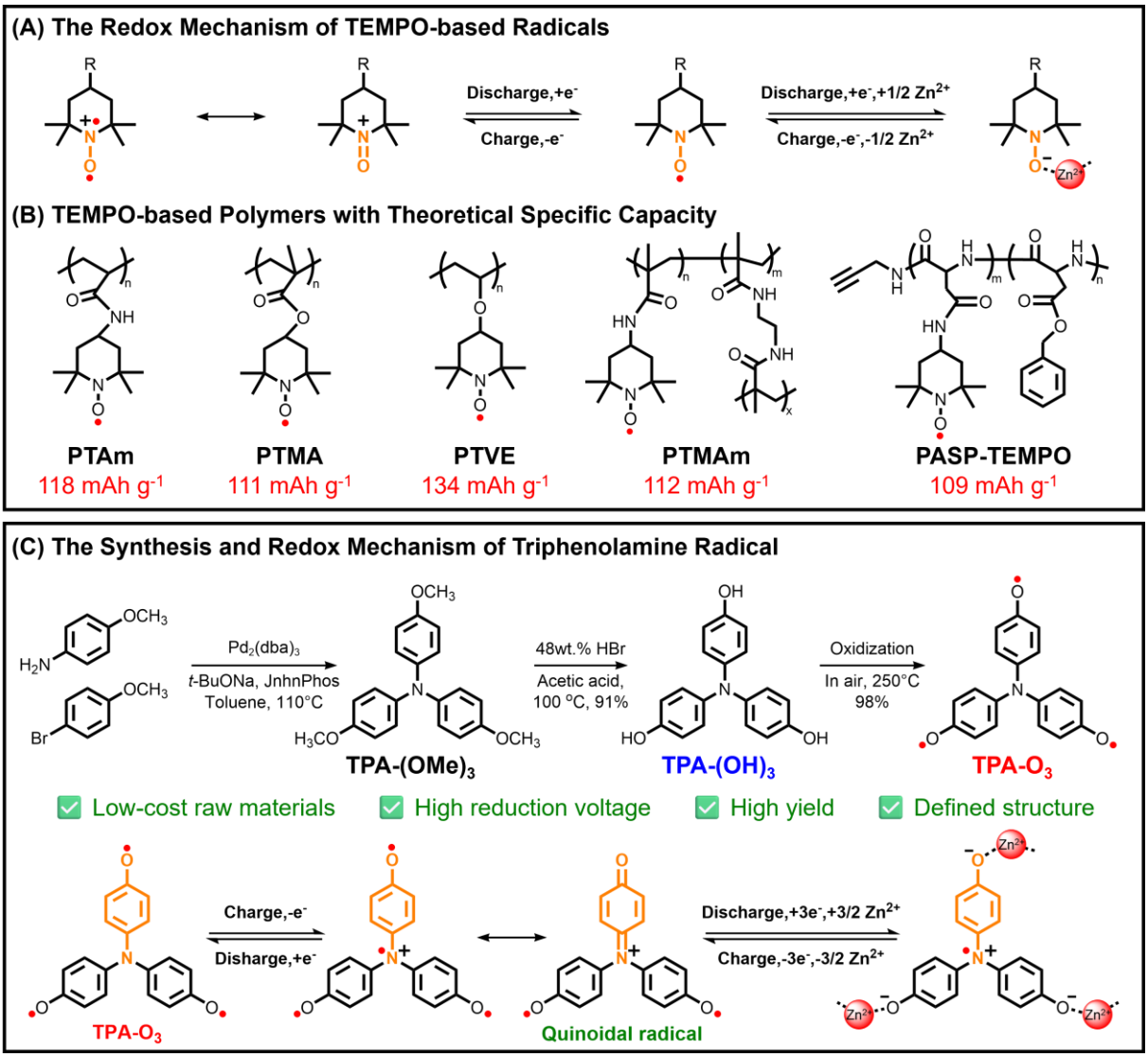

Figure 1. (A) The redox mechanism of TEMPO-based radical. (B)The previously reported TEMPO-based polymer cathodes with theoretical specific capacities. (C) The synthesis and redox mechanism of TPA radical.

(TEMPO) radical system (**Figures 1A** and **1B**[3b,19]).[20] One the other hand, enhancing π conjugation to delocalize radicals and modulate electronic structures is a reliable and efficient design paradigm to stabilize radicals.[12l] The spin density of radical molecules can be extensively delocalized on the π-conjugated network and multiple resonance structures.[12l] Since 2017, our group has been devoted to developing the triphenylamine derivatives and radicals, such as the TBP-OH_4, TPD-OH_4 and Spiro-OH_8.[21] In our recent work, the aromatic nitric acid radicals (ANARs) that do not require protection from bulky hindering groups have been reported for the first time by our group and showed excellent photothermal stability in air.[12i,12j,20-22] Such ANARs can be considered as a class of aromatized nitric acid derivatives and their closed-shell resonance structures are strikingly similar to those of nitro groups,[12g-

[j,12l,22] which contribute the stability of these radical molecules. In addition, unpaired electrons can be stabilized via delocalization into the conjugated skeleton, thereby reducing spin density. More importantly, the ANARs system possesses active sites of nitrogen atoms and phenol radicals, which can efficiently combine with Zn^{2+} in the cathode reaction, and thus, makes it a promising candidate for aqueous ZIBs cathode materials.

Herein, based on the ANARs strategy, TPA-$(OH)_3$ was synthesized via two simple steps and facile purification using extremely low-cost raw materials. Then, the ANAR radical TPA-O_3 were facilely prepared from a simple heating treatment of TPA-$(OH)_3$ powder at 250 °C in air (**Figures 1C** and **S1**). The TPA-O_3 can be considered as ANAR, so the reaction mechanisms of TPA-O_3 with zinc ion are very similar to TEMPO (**Figures 1A** and **1C**). The difference is that TPA-O_3 does not require large steric hindrance groups to protect the phenol radicals comparing with TEMPO, which greatly increases the theoretical specific capacities. The phenol radicals in TPA-O_3 can be well delocalized on the phenyl ring along with the formation of quinoidal structure under the driving force of aggregation-induced radical (AIR) effect, that is, the quinoidal character of molecule is greatly enhanced and free electrons are stabilized in the aggregated state accompanied with the boosted delocalization and pancake bond formation.[12h,12m,23] Usually, the organic radicals are reported to display higher electron conductivity compared to their precursors,[12l,24] which is also confirmed in TPA-O_3 (3.35×10^{-4} S cm^{-1}) and TPA-$(OMe)_3$ (2.73×10^{-6} S cm^{-1}). Additionally, multiple resonance structures of TPA-O_3, including quinoidal structures and nitro-like structures, are also one of the driving forces for its stability, which ensures a high electron conductivity and high-rate properties during the battery cycle.[22] Compared with the structures of our previously published ANARs,[12f,12i,12j,22,23b] TPA-O_3 is one of the simplest and cost-effective ANARs, which has a great cost advantage for aqueous Zn-organic batteries. We carefully unveil the ionic storage mechanisms in TPA-O_3 through electron spin resonance, X-ray photoelectron spectroscopy and fourier transform infrared and reveal the pivotal contribution to the fabrication of organic radical-based aqueous ZIBs. As a result, TPA-O_3 cathode display high reduction voltage of 1.02~1.33 V, desirable rate capability and high-capacity retention of 95.87% after 2000 stable long-term cycle at 5 A g^{-1} with the capacities of 123.7 mAh g^{-1}. These results indicate that the ANARs has great application potential in aqueous ZIBs with high cyclability and superior rate performance.

2. Results and discussion

The TPA-$(OMe)_3$, TPA-$(OH)_3$ and TPA-O_3 were readily prepared via two-step high yield reaction with low cost raw materials and simple purification according our previous work published in 2017.[12j,21-22] Although TPA-$(OH)_3$ has been studied as a catholyte for zinc–organic aqueous redox flow batteries by prof. Loh in 2021,[25] our group was the first to develop the system based on TPA-$(OH)_3$ and related compounds, and they did not cite our previous research work published in 2017 and 2019.[21-22] Moreover, the work in the current article with the TPA-$(OH)_3$ and TPA-O_3 used as cathode materials for aqueous ZIBs is rarely reported to date. Their chemical structures, optical properties, and electrical properties were carefully characterized and confirmed by the $^1H/^{13}C$ nuclear magnetic resonance (NMR), high-resolution matrix-assisted laser desorption/ionization time-of-flight (MALDI-TOF) mass, UV-vis absorption, photoluminescence (PL), fourier transform infrared spectroscopy (FTIR) and cyclic voltammetry (CV) spectra (**Figures S1-S14**, **Supporting Information**).

The UV-Vis spectra of TPA-$(OH)_3$ and TPA-O_3 in solution and film states were recorded to study the optical properties. However, we failed to record the UV-Vis absorption spectrum of TPA-$(OMe)_3$ film due to its poor film formability. In **Figures 2A** and **S11**, the UV-Vis absorption spectrum of TPA-O_3 is very similar to that of TPA-$(OH)_3$ in DMSO, indicating that the TPA-O_3 is protonated with the trace water in solvent, which have been disclosed in our previous reported work.[12g,12i,12j] Interestingly, compared with the TPA-$(OH)_3$, TPA-O_3 as the oxidized product of TPA-$(OH)_3$ exhibited a much broader characteristic absorption spectrum in thin film between 500 and 900 nm due to the aggregation effect.[22-23] It can also be found that the TPA-O_3 displayed a more extended optical absorption edge (around 880 nm) than those of TPA-$(OMe)_3$ and TPA-$(OH)_3$, which is consistent with our previous work that radical species usually display broadening absorption spectra.[12i,12j] Based on the optical absorption edge, the optical bandgaps of TPA-$(OMe)_3$, TPA-$(OH)_3$ and TPA-O_3 are calculated to be 3.20 eV, 3.10 eV and 1.40 eV, respectively, and the sharply narrowed bandgap of TPA-O_3 is one of the typical feature of ANARs, which contributes to its high electron conductivity of 3.35×10^{-4} S cm^{-1} as well as high-rate performance in ZIBs.

The PL test is applied to disclose the optical characters of TPA-$(OMe)_3$, TPA-$(OH)_3$ and TPA-O_3. The materials with a concentration of 6 mg mL^{-1} in ethyl acetate were spin-coated on the silica glass to prepare the thin films. In **Figure S12**, the PL emission peaks around 394 nm were detected in the TPA-$(OMe)_3$ and TPA-$(OH)_3$ under excitation wavelength of 300 nm, while the PL of TPA-O_3 is almost quenched under the same condition. This result can be attributed to the radiative channel forbiddance and non-radiative channel permission of

radical.[22-23] Regardless of the UV or PL test, TPA-O_3 radical showed extremely different optical properties from those of TPA-$(OMe)_3$ and TPA-$(OH)_3$, which can be ascribed to the neutral oxygen radical structures and unique electronic resonance structures of TPA-O_3 (see the inset in **Figure 2B**), which could provide abundant zinc ion active sites in aqueous ZIBs.

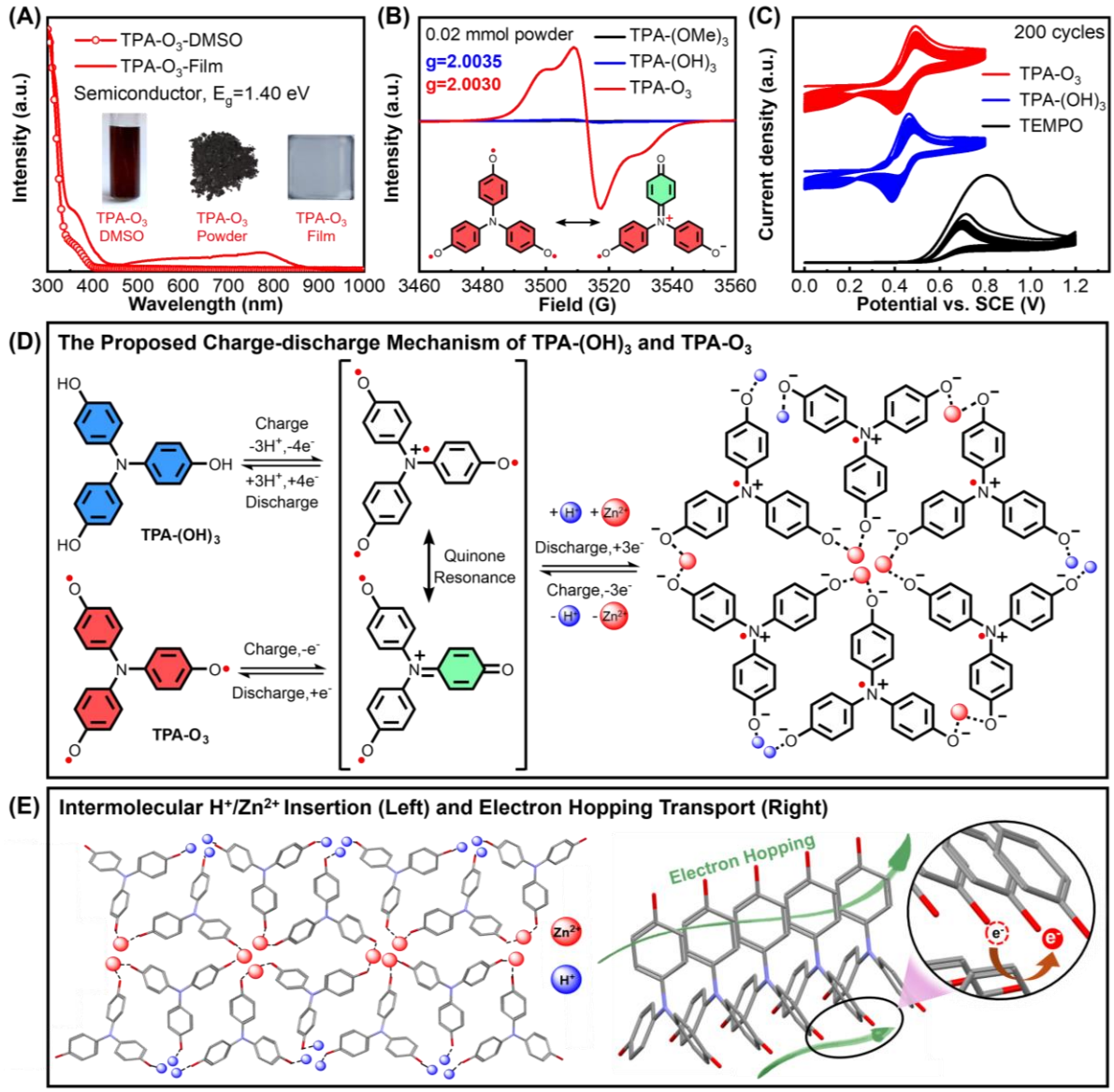

Figure 2. (A) Ultraviolet absorption spectra of TPA-O_3 molecules. Insets are the TPA-O_3 in solution, powder and film state, respectively. (B) ESR spectra of TPA-$(OMe)_3$, TPA-$(OH)_3$ and TPA-O_3 molecules in powder state (0.02 mmol). (C) Cyclic voltammetry of TPA-$(OH)_3$, TPA-O_3 and TEMPO radical in DMSO solvent (200 cycles). (D) The proposed charge-discharge mechanism of triphenolamine radical cathode in aqueous ZIBs. The benzene ring in green represents the quinoidal structure. (E) The proposed Zn^{2+}/H^+ insertion mechanism and electronic conductivity of triphenolamine radical based on the single crystal data.

The FTIR was carried out to further confirm the radical structure of TPA-O_3 with functional group changes comparing with its precursors. In **Figure S13**, TPA-$(OMe)_3$ shows stretch vibration peaks of O-H (3600-3200 cm^{-1}), characteristic sp^3 C-O (around 1030 cm^{-1}) and sp^3 C-H (around 2950 cm^{-1}), which are attributed to the trace water vapor, sp^3 C-O and sp^3 C-H bond of the methoxy groups, respectively. After demethylation, the enhanced O-H signal peak (attributed to phenol hydroxyl groups) of TPA-$(OH)_3$ appears and the characteristic sp^3 C-O and sp^3 C-H peak of the methoxy groups disappears. For the TPA-O_3, an absorption peak at 3250 cm^{-1} different from the phenol hydroxyl group appears and can be classified as the characteristic peak of phenol radicals (Ph-O·). Furthermore, the generation of phenol radicals was evidenced by the electron spin resonance (ESR) spectroscopy. 0.02 mmol TPA-$(OMe)_3$, TPA-$(OH)_3$ and TPA-O_3 powders were placed in the NMR tube respectively and the paramagnetic signal was measured at room temperature to reveal the electronic structure (**Figure 2B**). Compared with the negligible ESR signal of TPA-$(OMe)_3$ and TPA-$(OH)_3$, TPA-O_3 displayed a strong spin concentration with typical g value of 2.0030 due to the highly delocalized phenol radicals on the backbone of TPA-O_3, which indicates that TPA-O_3 possesses an intrinsic open-shell carbon radical, rather than localized phenoxy radical with g value of 2.0060.[22-23] Among them, there is a clear splitting peak of TPA-O_3, which is caused by the resonance structure with positive N cation radical, resulting in free electrons located near nitrogen positive ions.[26]

The CV test was conducted to study the energy levels and electrochemical characters (**Figures 2C** and **S14**). In the 200-cycle CV test in ambient condition (**Figure 2C**), TPA-$(OH)_3$ and TPA-O_3 maintained quasi-reversible CV spectra, while the TEMPO radical showed irreversible CV behaviour in the 200-cycle test, illustrating TPA-$(OH)_3$ and TPA-O_3 with superior redox stability are more suitable to act as cathode materials for aqueous ZIBs. Then, the highest (lowest) occupied (unoccupied) molecular orbital (HOMO (LUMO)) energy levels are calculated based on the initial oxidation potential and the optical band gap, and the details are presented in **Table S2**. Compared with TPA-O_3 (-4.81 eV), TPA-$(OH)_3$ (-4.79 eV) with shallower HOMO shows higher reactivity with oxygen and is easier to be dehydrogenated via heat treatment to transform into TPA-O_3 in air, thus the oxidation products of TPA-O_3 exhibits a deeper HOMO energy level.

Compared with the reported TEMPO-based radical cathode materials in **Figure 1B**, TPA-$(OH)_3$ and TPA-O_3 molecules show much higher theoretical specific capacity due to their multi-electron charge-discharge mechanism and low molecular weight (**Figures 2D** and **5B**). Referring to the single crystal structure shown in **Figure 2E**,[25] TPA-$(OH)_3$ molecules are

regularly arranged through strong hydrogen bonds, and this network provides the ion channel for the transport of zinc ions. Similarly, with the high electron conductivity of 3.35×10^{-4} S cm^{-1}, the electron transport in TPA-O_3 cathode will be efficient via the electron hopping mechanism between the tightly packed molecules,[27] contributing to its high rate performance in aqueous ZIBs. For the TPA-$(OMe)_3$ cathode without special electron delocalization, its lower conductivity (2.73×10^{-6} S cm^{-1}) leads to poor battery performance. Based on the subtle difference between TPA-O_3 and TPA-$(OH)_3$, their mutual conversion process and ion deintercalation during redox reactions are presented in **Figure 2D**. After charging, TPA-$(OH)_3$ and TPA-O_3 were converted into radical cations, which will stabilize the phenol radicals via their quinoidal resonance structures. Meanwhile, the electron-deficient central nitrogen cation exhibits stronger electron-withdrawing effect to phenol radicals, greatly promoting the delocalization of phenol radicals and reduces the local electron spin density, thereby realizing the reversible storage of Zn^{2+} and H^+.[12i,21-22] The stability of radical in air, reversible behaviour in CV, and multi-electron transfer and ion storage mechanism of TPA-O_3 are rarely reported in radical cathodes, indicating the great potential of TPA-O_3 system as cathode materials for high rate and capacity battery.[12l]

To demonstrate the potential of TPA-$(OH)_3$ and TPA-O_3 radical as energy storage materials, their electrochemical properties as cathodes were tested. The CR2032 coin-type cell was selected to assemble zinc ion battery with TPA-$(OH)_3$ or TPA-O_3 cathode, zinc foil anode and 2.0 M $ZnSO_4$ aqueous electrolyte. **Figures 3A-3C** show the voltage distribution and capacity evolution at different current densities of TPA-$(OH)_3$ and TPA-O_3, and they both have excellent multiplier performance, with the cathode still exhibiting high capacity as the current density increases. Specifically, the TPA-$(OH)_3$ displays specific capacities of 137.7, 132.2, 125.7, 119.8, and 116.4 mAh g^{-1} at a current density of 2, 3, 5, 8 and 10 A g^{-1}, while the capacities of TPA-O_3 are 149.9, 144.3, 137.7, 130.7 and 127.0 mAh g^{-1} at the same current density. Furthermore, the TPA-$(OH)_3$ and TPA-O_3 cathodes achieve a high discharge voltage of 1.02-1.33 V, which is largely higher than reported organic cathodes such as quinone cathodes.[28] The electrochemical results validate the feasibility of TPA-O_3 as a cathode material for aqueous ZIBs. In addition, 2000 stable cycles were achieved at 5 A g^{-1} with a capacity decay rate of 2.03 % and 4.13 % for TPA-$(OH)_3$ and TPA-O_3, respectively (**Figure 3D**). The negligible capacity decay in long cycling tests proves the amazing stability of the organic radical TPA-O_3, thanks to the delocalization effect of aromatic rings on radical electrons. At a current density of 5 A g^{-1}, the galvanostatic (dis-)charge curves remain stable and reversible from cycle 1 to cycle 2000, indicating the good electrochemical stability of the TPA-$(OH)_3$ and TPA-O_3 cathodes

(**Figure 3E-3F**). As shown in **Figure 3G**, TPA-O_3 displays a high capacity after 2000 stable cycles at 5 A g^{-1}, which is superior to most reported TEMPO-based radical or quinone cathode (**Table S3** and **S4**).

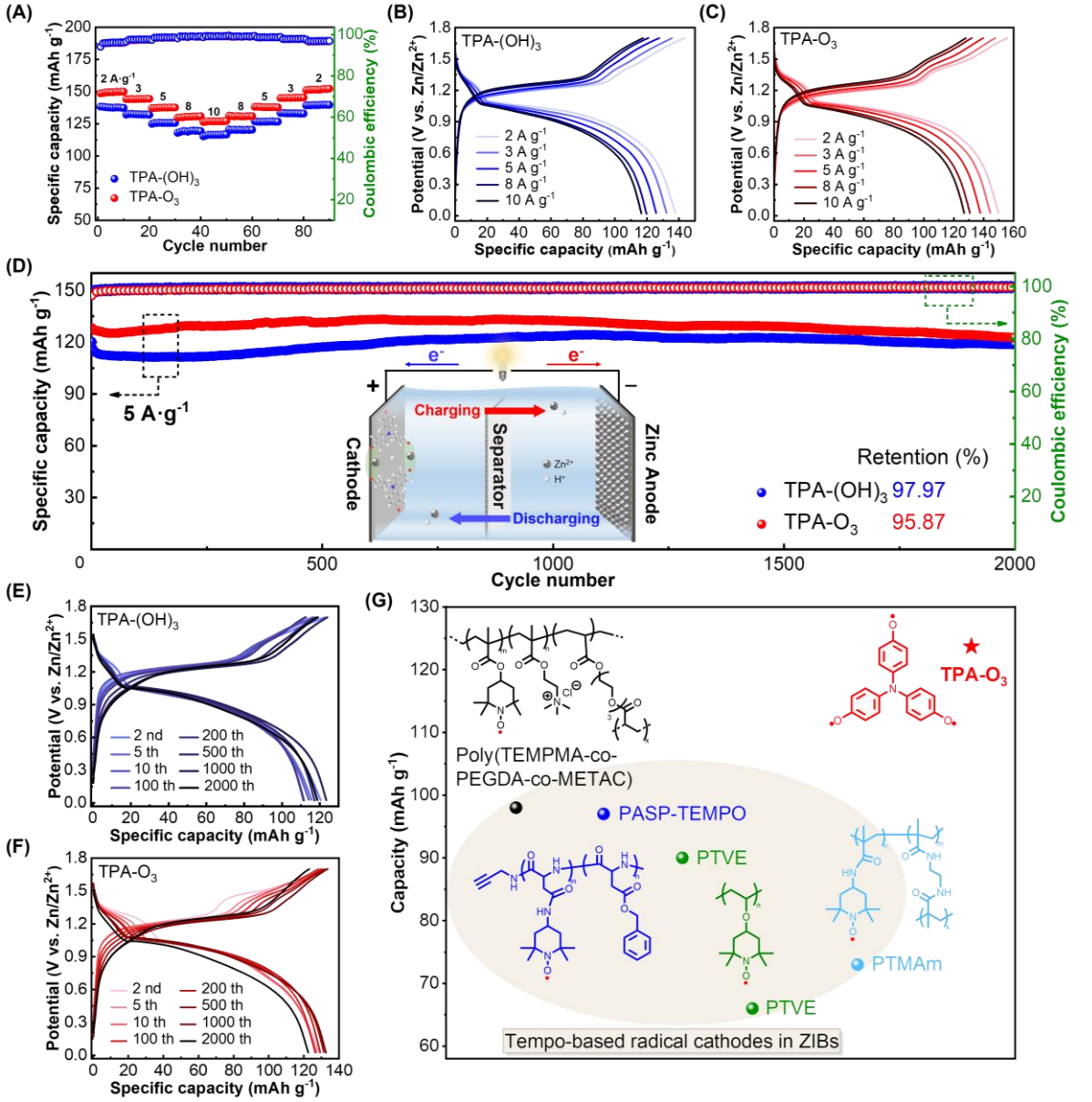

Figure 3. (A) Rate specific capacity of TPA-$(OH)_3$ and TPA-O_3 at different current densities and the corresponding coulombic efficiency. (B-C) Rate (dis-)charge curves of TPA-$(OH)_3$ and TPA-O_3 at different current densities. (D) Cycling stability and coulombic efficiency of TPA-$(OH)_3$ and TPA-O_3 at 5 A g^{-1}. The inset is the ZIB structure diagram. (E-F) Galvanostatic discharge/charge curves of TPA-$(OH)_3$ and TPA-O_3 at 5 A g^{-1}. (G) Long cycling performance of the reported organic radical cathodes for aqueous ZIBs. The numbers are used to distinguish different compounds and the detailed information can be obtained in Table S3.

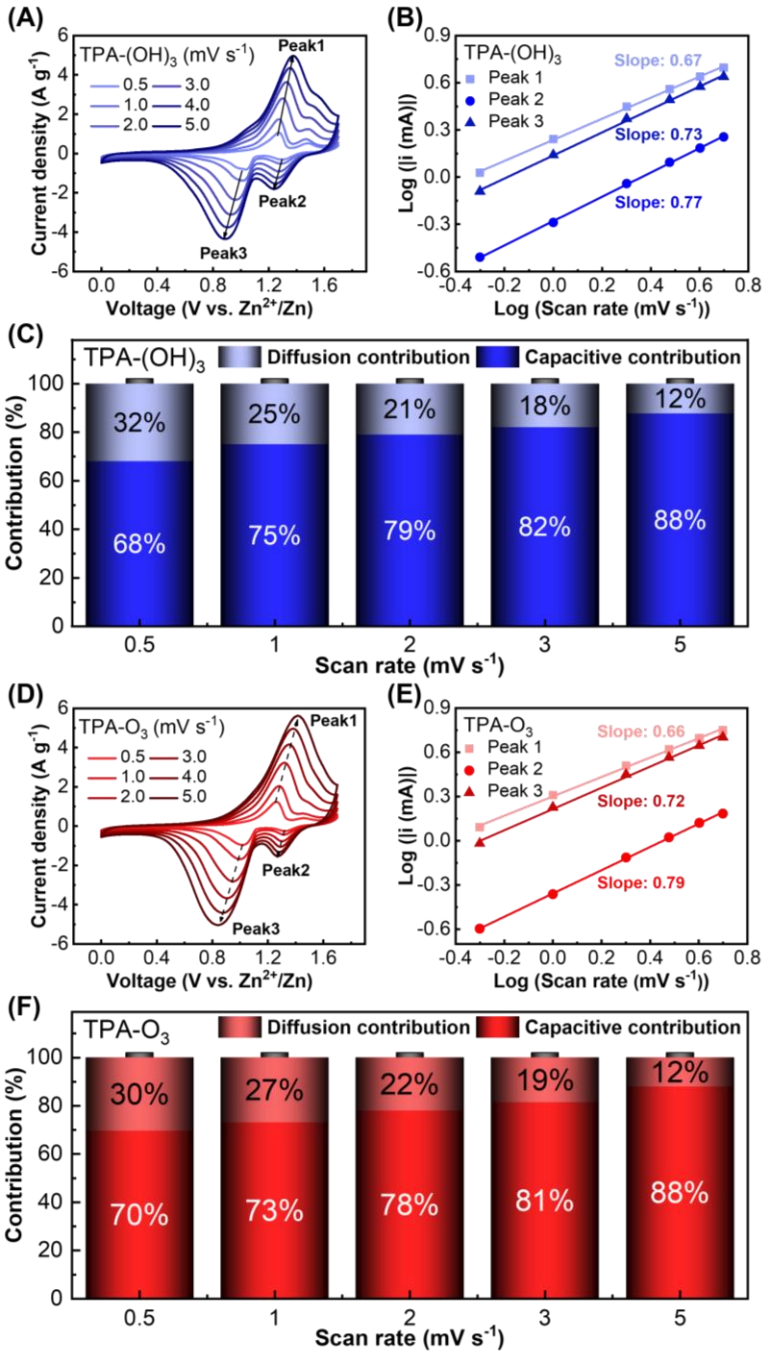

Figure 4. (A,D) CV curves of TPA-$(OH)_3$ and TPA-O_3 in a three-electrode cell with 2 M $ZnSO_4$ electrolyte at scan rates (v) from 0.5 to 5.0 mV s^{-1}. (B,E) Relationship between the peak current (i) and sweep rate (v): logi–logv in CV at scan rates of 0.2–100 mV s^{-1}. (C,F) Capacitive and diffusion-controlled capacity contribution of TPA-$(OH)_3$ and TPA-O_3 cathodes at different scan rates.

To investigate the relationship between performance and electrochemical kinetics of TPA-$(OH)_3$ and TPA-O_3, CV curves were recorded at different scan rates of 0.5, 1, 2, 3, 4 and 5 mV s^{-1} (**Figures 4A** and **4D**). The overpotential of redox pairs in TPA-OH_3 and TPA-O_3 increases

only slightly with increasing scan rate. In general, the peak current i in CV is related to the scan rate v as: $i = av^b$. b values can be calculated from the linear relationship logi-logv. As shown in the **Figures 4B** and **4E,** both TPA-$(OH)_3$ and TPA-O_3 cathodes show an oxidation peak b value > 0.65 and a reduction peak b value > 0.7, indicating that the contribution of the cation embedding/stripping is the dominant capacitance-controlled process. In addition, the diffusion control contribution and the capacitive contribution in the cell system can be quantified separately (**Figures 4C** and **4F**). The capacitive contributions of TPA-$(OH)_3$ and radical TPA-O_3 are shown in **Figures S18**-**S19**, respectively, as the ratio of the capacitive contributions to the total capacity, and the capacitive contributions increase with the accelerated sweep speed. The TPA-$(OH)_3$ cathode has a capacitive contribution of 68% at a scan rate of 0.5 mV s^{-1}, which increases further to 88% at 5.0 mV s^{-1}. Similar results are obtained for the TPA-O_3 cathode, with a capacitive contribution of 70% at a scan rate of 0.5 mV s^{-1}, increasing to 88% at 5.0 mV s^{-1}. The results are in agreement with the conclusions drawn from the above analysis of the b-values. There is no doubt that the fast pseudocapacitance process confers superior multiplicative performance to this radical organic cell system.

We then investigated the detailed charge storage chemistry of the TPA-$(OH)_3$ and TPA-O_3 cathodes. The cathodes in 2.0 M $ZnSO_4$ electrolyte with different charge/discharge depths were selected for a series of ex-situ characterisations. The ESR of the electrodes was recorded to understand the reaction mechanism through identifying the variations of the g-values of radical intermediate during the redox reaction process. In **Figure 5A**, the hyperfine structures of pristine electrodes of TPA-$(OH)_3$ and TPA-O_3 are eliminated due to the delocalization of phenol radicals,[12i,12j] and the g-values are close to the reported triphenylamine radical cations ($[(C_6H_5)_3N\cdot]^+$) (around 2.0030).[26] After the first charge (1Ch), both the significantly improved ESR signal of TPA-$(OH)_3$ and TPA-O_3 is caused by the formation of $[(C_6H_4O\cdot)_3N\cdot]^+$ positive cation radical in the oxidation (2.0026 for TPA-$(OH)_3$ and 2.0027 for TPA-O_3). As the discharge depth increases, the phenol radicals were reduced into radical anions, and thus causing a gradual weakening of ESR signals for TPA-$(OH)_3$ and TPA-O_3. Importantly, both TPA-$(OH)_3$ and TPA-O_3 show g-value around 2.0028 during the redox processes, revealing that the molecule always retains a central nitrogen positive cation radical structure (**Figure 5B**), which confirms the three-electron transfer mechanism of TPA-$(OH)_3$ and TPA-O_3. In the second charging process, the ESR signal of TPA-O_3 shows an increasing trend along with a negligible change in g-value of 2.0030, while the spin intensity of TPA-$(OH)_3$ is almost silent, indicating greater irreversibility of the TPA-$(OH)_3$ electrode. This result is consistent with the minimal capacity decay of TPA-O_3 (4.13 %) in long cycling testing.

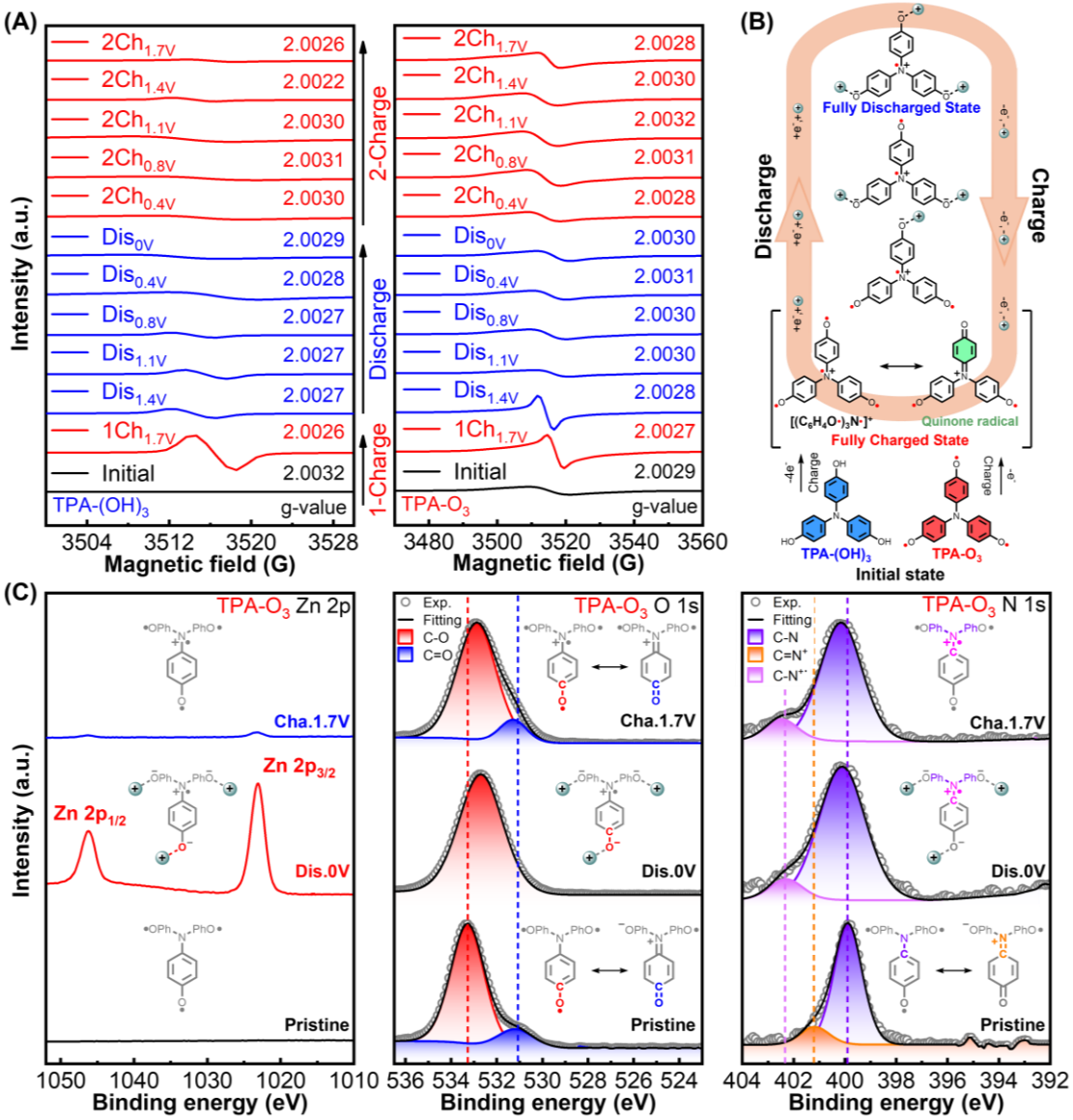

Figure 5. (A) ESR spectra of TPA-$(OH)_3$ and TPA-O_3 electrodes with different charging and discharging depths. (B) The three-electron redox process of TPA-$(OH)_3$ and TPA-O_3 in the charge-discharge process. (C) The XPS spectra of TPA-O_3 cathode in pristine state, fully charged state and fully discharged states. The colored covalent bonds correspond to the XPS peaks with the same colour.

Furtherly, the ion storage mechanism of TPA-O_3 was deeply confirmed via X-ray photoelectron spectroscopy (XPS). In **Figure 5C**, the Zn 2p spectra show a strong signal at fully discharged state (Dis.$_{0V}$), and the relative intensity was significantly weakened upon charging, indicating the occurrence of uptake of Zn^{2+} upon discharge and removal upon charging, which also means that the Zn^{2+} is involved in the reversible ion storage. In addition, the C-O bond peak shifts to the lower binding energy from pristine state to Dis.$_{0V}$, indicating that the radicals were reduced during discharge and can bind with Zn^{2+}. After reaching the fully

charged state (Cha.$_{1.7V}$), the C-O bond peak approaches the peak of pristine state again, and the phenol radical anions were oxidized along with the recovery of neutral TPA-O_3 radical. The higher C=O signal in the pristine state originates from the quinoidal resonance structure of TPA-O_3 (see the inset in **Figure 5C**). Obviously, the C=O peak completely disappears in Dis.$_{0V}$, indicating that all the phenol anions reacted with Zn^{2+} cations and unable to resonate to the quinoidal structures. Interestingly, the C=O peak reappears in Cha.$_{1.7V}$, demonstrating the reversible storage of Zn^{2+} cations. For the N-1s spectra, the quinoidal resonance structure of TPA-O_3 results in a C=N^+ peak (401.2 eV) at the pristine electrode, while the Cha.$_{1.7V}$ and Dis.$_{0V}$ states exhibited shifting C-$N^{+\cdot}$ peaks.[29] The C-N peak displays a shift toward a higher binding energy from the pristine to the Dis.$_{0V}$ and Cha.$_{1.7V}$ state, implying the production of central nitrogen positive cation radical. More importantly, the position of the C-N and C-$N^{+\cdot}$ peaks almost unchanged during the charging and discharging process, proving that nitrogen positive cation radical always present in redox process, which is consistent with the electrode ESR results (**Figure 5A**), and supports the extremely reversible three-electron transfer mechanism in charge-discharge as well as Zn^{2+} storage and transport process (**Figure 5B**).

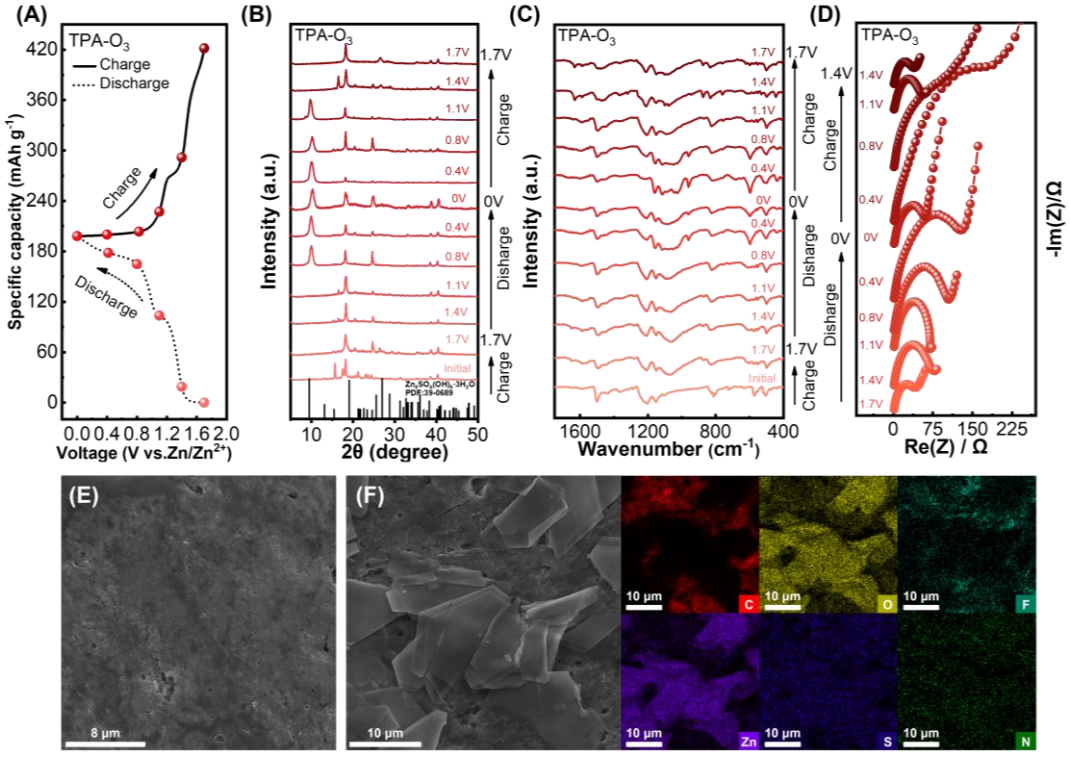

Figure 6. (A) Galvanostatic charge–discharge curves of TPA-O_3 cathode with different charge-discharge depths in 2.0 M $ZnSO_4$ electrolyte. (B) Ex situ XRD diffractograms, (C) FTIR spectrum, (D) In situ EIS profiles of TPA-O_3 electrode at different charge-discharge states. (E) SEM image of charged 1.7 V TPA-O_3 cathode (F) SEM image and EDS mapping of discharged 0V TPA-O_3 cathode.

To further understand the phase evolution of TPA-O_3 electrode, ex-situ X-ray diffraction (XRD), FTIR and electrochemical impedance spectroscopy (EIS) tests were conducted. The galvanostatic charge-discharge curves were shown in **Figure 6A**. **Figure 6B** shows an ex-situ XRD diffraction pattern of the TPA-O_3 electrode, with characteristic peaks at 9.7°, 28.6° and 33.1° appearing gradually during the discharge. The characteristic peak at this position is attributed to zinc hydroxide sulphate hydrate ($Zn_4SO_4(OH)_6$-$3H_2O$ (JCPDS:39-0689), which disappears during charging. Similar charge/discharge curves and XRD curves of the cathode as a function of voltage also occur for TPA-$(OH)_3$ (**Figures S20** and **S22**). The production of this substance usually indicates that H^+ are embedded with Zn^{2+} during the discharge and charge process. This is because the consumption of H^+ results in a weakly alkaline solution on the electrode surface and $ZnSO_4$ is converted to $Zn_4SO_4(OH)_6$-$3H_2O$ in this environment, which is also observed in previous work.[30]

To further demonstrate the involvement of protons in the charge storage process, we tested the CV curves of TPA-$(OH)_3$ and TPA-O_3 in 1 M H_2SO_4 and 2 M $ZnSO_4$ electrolytes using a three-electrode system with Pt as counter electrode and Ag/AgCl as reference electrode. In 1M H_2SO_4 electrolyte, both materials showed a reduction peak located at 0.48 V followed by an oxidation peak at 0.5 V by cyclic voltammetric scanning. In 2M $ZnSO_4$ electrolyte, two reduction peaks at around 0.08 V and 0.35 V and oxidation peaks at around 0.19 V and 0.42 V were observed for both TPA-$(OH)_3$ and TPA-O_3. The CV curves measured in 1 M H_2SO_4 electrolyte were shifted according to the Nernst equation, in which the positions of the reduction peaks and oxidation peaks overlapped with those measured in 2 M $ZnSO_4$ (**Figures S16** and **S17**). This result confirms the involvement of both H^+ and Zn^{2+} in charge storage.[28b]

The FTIR spectra of the TPA-O_3 and TPA-$(OH)_3$ electrode at different states of discharge and charge are shown in **Figures 6C** and **S23,** respectively. During discharge, a new absorption peak at 598 cm^{-1} appears, which is attributed to Zn-O,[12e] while a new adsorption peak attributed to the S=O group also appears at 959 cm^{-1}, which is attributed to the formation of basic zinc sulfate by-product.[31] During discharge, a new absorption peak at 598 cm^{-1} appears, which is attributed to O-S-O, while a new adsorption peak attributed to the S-O group also appears at 959 cm^{-1}. Interestingly, both peaks disappear during the charging process. This phenomenon indicates that, $Zn_4SO_4(OH)_6$-$3H_2O$ was generated during discharge and disappeared during charging, which is consistent with the XRD results. At the same time, the charge transfer resistance measured by EIS shows that the impedance increases during the discharge process and recovers at the end of the charge (**Figures 6D** and **S21**), verifying the reversible formation of $Zn_4SO_4(OH)_6$-$3H_2O$. **Figures 6E** and **6F** shows the SEM results of the

surface of the TPA-O_3 electrode in the fully charged and fully discharged state respectively, the flaky $Zn_4SO_4(OH)_6$-$3H_2O$ product can be clearly observed on the surface of the discharged electrode. The EDS energy spectra of the TPA-O_3 and TPA-$(OH)_3$ electrodes in the fully charged state are shown in **Figures S15A** and **S15C**, with a uniform distribution of C, O elements, which indicates that this area is uniformly coated with TPA-O_3 and TPA-$(OH)_3$, and there is a residue of Zn but no aggregation. As can be seen from the EDS image in **Figures 6F** and **S15**, the highlighted areas of the Zn, S and O elemental images match the lamellar areas observed in the SEM and can be identified as $Zn_4SO_4(OH)_6$-$3H_2O$. Therefore, the charge storage process of TPA-O_3 cathode involves the storage of both H^+ and Zn^{2+} cations.

3.Conclusions

In summary, we proposed an ultralow-cost organic radical material TPA-O_3 via simple two-step synthesis for high-performance aqueous ZIBs. The phenol radicals can be effectively stabilized through electron delocalization effect of three π-conjugated benzene ring structures. Importantly, the tight stacking and hydrogen bonding between molecules ensure the transport of ions and electrons ($\sigma = 3.35\times10^{-4}$ S cm^{-1}). As a result, TPA-$(OH)_3$ and TPA-O_3 cathode deliver capacities of 119.4 mAh g^{-1} and 123.7 mAh g^{-1} at 5 A g^{-1} after 2000 long-term cycles, respectively, and outstanding rate capability, which exceeds most TEMPO-based and quinone-based cathode materials. This work offers in-depth insights into the storage mechanism of TPA-O_3 radical cathode and pave the way for the potential application of radical cathodes in aqueous ZIBs.

Acknowledgements

J.H. and M.L. contributed equally to this work. The work was financially supported by the Natural Science Foundation of China (51973063, 22375065, 22279160), and the Fund of Guangdong Provincial Key Laboratory of Luminescence from Molecular Aggregates (2019B030301003).

Conflict of Interest Statement

The authors have no conflicts of interest to declare.

Received: ((will be filled in by the editorial staff))
Revised: ((will be filled in by the editorial staff))
Published online: ((will be filled in by the editorial staff))

References

[1] M. Armand, J. M. Tarascon, *Nature* **2008**, *451*, 652–657.

[2] Q. Zhao, Y. Lu, J. Chen, *Adv. Energy Mater.* **2017**, *7*, 1601792.

[3] a) J. F. Parker, C. N. Chervin, I. R. Pala, M. Machler, M. F. Burz, J. W. Long, D. R. Rolison, *Science* **2017**, *356*, 415; b) Y. Deng, C. Teng, Y. Wu, K. Zhang, L. Yan, *ChemSusChem* **2022**, *15*, e202102710; c) J. Zhu, Z. Bie, X. Cai, Z. Jiao, Z. Wang, J. Tao, W. Song, H. J. Fan, *Adv. Mater.* **2022**, *34*, e2207209; d) D. Chao, C. R. Zhu, M. Song, P. Liang, X. Zhang, N. H. Tiep, H. Zhao, J. Wang, R. Wang, H. Zhang, H. J. Fan, *Adv. Mater.* **2018**, *30*, e1803181; e) F. Wang, J. Zhang, H. Lu, H. Zhu, Z. Chen, L. Wang, J. Yu, C. You, W. Li, J. Song, Z. Weng, C. Yang, Q. H. Yang, *Nat. Commun.* **2023**, *14*, 4211; f) Z. Tie, Z. Niu, *Angew. Chem. Int. Ed.* **2020**, *59*, 21293-21303; g) L. Wang, Z. Wang, H. Li, D. Han, X. Li, F. Wang, J. Gao, C. Geng, Z. Zhang, C. Cui, Z. Weng, C. Yang, K. P. Loh, Q. H. Yang, *ACS Nano* **2023**, *17*, 668-677.

[4] a) H. Yang, W. Zhou, D. Chen, J. Liu, Z. Yuan, M. Lu, L. Shen, V. Shulga, W. Han, D. Chao, *Energy Environ. Sci.* **2022**, *15*, 1106-1118; b) X. Li, C. Ji, J. Shen, J. Feng, H. Mi, Y. Xu, F. Guo, X. Yan, *Adv. Sci.* **2023**, *10*, e2205794; c) Y. Zeng, Y. Wang, Q. Jin, Z. Pei, D. Luan, X. Zhang, X. W. D. Lou, *Angew. Chem. Int. Ed.* **2021**, *60*, 25793-25798; d) H. Yang, T. Zhang, D. Chen, Y. Tan, W. Zhou, L. Li, W. Li, G. Li, W. Han, H. J. Fan, D. Chao, *Adv. Mater.* **2023**, *35*, e2300053; e) J. Sun, Z. Liu, K. Li, Y. Yuan, X. Zheng, Y. Xu, M. Wang, M. Chuai, H. Hu, W. Chen, *ACS Appl. Mater. Interfaces* **2022**, *14*, 51900-51909.

[5] a) Y. Liu, Y. Jiang, Z. Hu, J. Peng, W. Lai, D. Wu, S. Zuo, J. Zhang, B. Chen, Z. Dai, Y. Yang, Y. Huang, W. Zhang, W. Zhao, W. Zhang, L. Wang, S. Chou, *Adv. Funct. Mater.* **2020**, *31*, 2008033; b) X. Wang, Y. Wang, Y. Jiang, X. Li, Y. Liu, H. Xiao, Y. Ma, Y. y. Huang, G. Yuan, *Adv. Funct. Mater.* **2021**, *31*, 2103210; c) D. Chen, M. Lu, B. Wang, H. Cheng, H. Yang, D. Cai, W. Han, H. J. Fan, *Nano Energy* **2021**, *83*, 105835; d) X. Ma, X. Cao, M. Yao, L. Shan, X. Shi, G. Fang, A. Pan, B. Lu, J. Zhou, S. Liang, *Adv. Mater.* **2022**, *34*, e2105452; e) P. Wang, X. Shi, Z. Wu, S. Guo, J. Zhou, S. Liang, *Carbon Energy* **2020**, *2*, 294-301; f) K. Yang, Y. Hu, T. Zhang, B. Wang, J. Qin, N. Li, Z. Zhao, J. Zhao, D. Chao, *Adv. Energy Mater.* **2022**, *12*, 2202671; g) P. He, G. Zhang, X. Liao, M. Yan, X. Xu, Q. An, J. Liu, L. Mai, *Adv. Energy Mater.* **2018**, *8*, 1702463; h) L. Xing, C. Zhang, M. Li, P. Hu, X. Zhang, Y. Dai, X. Pan, W. Sun, S. Li, J. Xue, Q. An, L. Mai, *Energy Storage Mater.* **2022**, *52*, 291-298.

[6] a) F. Wang, Y. Li, W. Zhu, X. Ge, H. Cui, K. Feng, S. Liu, X. Yang, *ACS Appl. Mater. Interfaces* **2021**, *13*, 34468-34476; b) Y. Zeng, X. F. Lu, S. L. Zhang, D. Luan, S. Li, X. W. D. Lou, *Angew. Chem. Int. Ed.* **2021**, *60*, 22189-22194; c) Y. Zeng, J. Xu, Y. Wang, S. Li, D. Luan, X. W. D. Lou, *Angew. Chem. Int. Ed.* **2022**, *61*, e202212031.

[7] a) H. Zhang, Y. Fang, F. Yang, X. Liu, X. Lu, *Energy Environ. Sci.* **2020**, *13*, 2515-2523; b) D. Kundu, P. Oberholzer, C. Glaros, A. Bouzid, E. Tervoort, A. Pasquarello, M. Niederberger, *Chem. Mater.* **2018**, *30*, 3874-3881; c) Z. Tie, L. Liu, S. Deng, D. Zhao, Z. Niu, *Angew. Chem. Int. Ed.* **2020**, *59*, 4920-4924; d) F. Wan, L. Zhang, X. Wang, S. Bi, Z. Niu, J. Chen, *Adv. Funct. Mater.* **2018**, *28*, 1804975; e) L. Yan, Q. Zhu, Y. Qi, J. Xu, Y. Peng, J. Shu, J. Ma, Y. Wang, *Angew. Chem. Int. Ed.* **2022**, *61*, e202211107.

[8] S. Li, J. Shang, M. Li, M. Xu, F. Zeng, H. Yin, Y. Tang, C. Han, H. M. Cheng, *Adv. Mater.* **2022**, e2207115.

[9] J. Huang, Y. Li, R. Xie, J. Li, Z. Tian, G. Chai, Y. Zhang, F. Lai, G. He, C. Liu, T. Liu, D. J. L. Brett, *J. Energy Chem.* **2021**, *58*, 147-155.

[10] W. Sun, F. Wang, S. Hou, C. Yang, X. Fan, Z. Ma, T. Gao, F. Han, R. Hu, M. Zhu, C. Wang, *J. Am. Chem. Soc.* **2017**, *139*, 9775-9778.

[11] B. Tang, L. Shan, S. Liang, J. Zhou, *Energy Environ. Sci.* **2019**, *12*, 3288-3304.

[12] a) J.-M. Tarascon, M. Armand, *Nature* **2001**, *6861*, 359-367; b) M. Song, H. Tan, D. Chao, H. J. Fan, *Adv. Funct. Mater.* **2018**, *28*, 1802564; c) Y.-H. Zhang, Y. Li, *Rare Met.* **2021**, *40*, 2993-3018; d) N. Wang, X. Dong, B. Wang, Z. Guo, Z. Wang, R. Wang, X. Qiu, Y. Wang, *Angew. Chem. Int. Ed.* **2020**, *59*, 14577-14583; e) Y. Chen, J. Li, Q. Zhu, K. Fan, Y. Cao, G. Zhang, C. Zhang, Y. Gao, J. Zou, T. Zhai, C. Wang, *Angew. Chem. Int. Ed.* **2022**, *61*, e202116289; f) T. Niu, W. Zhu, Y. Zhang, Q. Xue, X. Jiao, Z. Wang, Y.-M. Xie, P. Li, R. Chen, F. Huang, Y. Li, H.-L. Yip, Y. Cao, *Joule* **2021**, *5*, 249-269; g) J. Huang, Z. Wang, W. Zhu, Y. Li, *Aggregate* **2024**, *5*, e426; h) J. Huang, C. Liao, L. Guan, Q. Meng, S. Gu, Z. He, Y. Li, *Chin. J. Chem.* **2024**; i) Z. Wang, J. Zhou, Y. Zhang, W. Zhu, Y. Li, *Angew. Chem. Int. Ed.* **2022**, *61*, e202113653; j) C. Chen, Q. Liang, Z. Chen, W. Zhu, Z. Wang, Y. Li, X. Wu, X. Xiong, *Angew. Chem. Int. Ed.* **2021**, *60*, 26718-26724; k) S. Fang, J. Huang, R. Tao, Q. Wei, X. Ding, S. Yajima, Z. Chen, W. Zhu, C. Liu, Y. Li, N. Yin, L. Song, Y. Liu, G. Shi, H. Wu, Y. Gao, X. Wen, Q. Chen, Q. Shen, Y. Li, Z. Liu, Y. Li, W. Ma, *Adv. Mater.* **2023**, *35*, 2212184; l) Z. X. Chen, Y. Li, F. Huang, *Chem* **2021**, *7*, 288-332; m) Z. Chen, W. Li, M. A. Sabuj, Y. Li, W. Zhu, M. Zeng, C. S. Sarap, M. M. Huda, X. Qiao, X. Peng, D. Ma, Y. Ma, N. Rai, F. Huang, *Nat. Commun.* **2021**, *12*, 5889; n) L. Yuan, W. Zhu, Y. Zhang, Y. Li, C. C. S. Chan, M. Qin, J. Qiu, K. Zhang, J. Huang, J.

Wang, H. Luo, Z. Zhang, R. Chen, W. Liang, Q. Wei, K. S. Wong, X. Lu, N. Li, C. J. Brabec, L. Ding, K. Yan, *Energy Environ. Sci.* **2023**, *16*, 1597-1609; o) W. Zhu, Z. Chen, J. Huang, W. Liang, C. Liao, J. Wang, T. Du, Y. Deng, G. Li, R. Chen, X. Peng, J. Hou, Y. Li, *J. Phys. Chem. C* **2023**, *127*, 8894-8903; p) J. Hou, O. Inganäs, R. H. Friend, F. Gao, *Nat. Mater.* **2018**, *17*, 119-128; q) S. Linic, U. Aslam, C. Boerigter, M. Morabito, *Nat. Mater.* **2015**, *14*, 567-576; r) G. Liu, J. Xu, K. Wang, *Nano Energy* **2017**, *41*, 269-284; s) L. Guan, J. Zou, M. Mao, C. Wang, *Acc. Mater. Res.* **2024**, *5*, 560-570; t) H. Dai, Y. Chen, Y. Gao, L. Gong, K. Fan, J. Zou, X. Wang, C. Zhang, M. Fu, G. Zhang, Y. Cao, C. Wang, *Adv. Energy Mater.* **2024**, *14*, 2304210; u) G. Zhang, L. Fu, Y. Chen, K. Fan, C. Zhang, H. Dai, L. Guan, M. Mao, J. Ma, C. Wang, *Adv. Mater.* **2024**, *36*, 2405949; v) P. Bai, X. Ji, J. Zhang, W. Zhang, S. Hou, H. Su, M. Li, T. Deng, L. Cao, S. Liu, X. He, Y. Xu, C. Wang, *Angew. Chem. Int. Ed.* **2022**, *61*, e202202731; w) W. Zhu, J. Zhang, J. Luo, C. Zeng, H. Su, J. Zhang, R. Liu, E. Hu, Y. Liu, W.-D. Liu, Y. Chen, W. Hu, Y. Xu, *Adv. Mater.* **2023**, *35*, 2208974; x) C. Yang, Z. Chen, C. Yu, J. Cao, G. Ke, W. Zhu, W. Liang, J. Huang, W. Cai, C. Saha, M. A. Sabuj, N. Rai, X. Li, J. Yang, Y. Li, F. Huang, X. Guo, *Nat. Nanotechnol.* **2024**, *19*, 978-985.

[13] a) S. Huang, F. Wan, S. Bi, J. Zhu, Z. Niu, J. Chen, *Angew. Chem. Int. Ed.* **2019**, *58*, 4313-4317; b) Hadrien Glatz, Erlantz Lizundia, Fiona Pacifico, D. Kundu, *ACS Appl. Energy Mater.* **2019**, *2*, 1288–1294.

[14] a) T. Suga, S. Sugita, H. Ohshiro, K. Oyaizu, H. Nishide, *Adv. Mater.* **2011**, *23*, 751-754; b) T. Janoschka, M. D. Hager, U. S. Schubert, *Adv. Mater.* **2012**, *24*, 6397-6409; c) H. Nishide, K. Oyaizu, *Science* **2008**, *319*, 737-738; d) Y. Morita, S. Nishida, T. Murata, M. Moriguchi, A. Ueda, M. Satoh, K. Arifuku, K. Sato, T. Takui, *Nat. Mater.* **2011**, *10*, 947-951; e) F. Kang, Y. Lin, S. Zhang, Z. Tan, X. Wang, J. Yang, Y.-K. Peng, W. Zhang, C.-S. Lee, W. Huang, Q. Zhang, *ACS Appl. Mater. Interfaces* **2023**, *15*, 9431-9438.

[15] I. Ratera, J. Veciana, *Chem. Soc. Rev.* **2012**, *41*, 303-349.

[16] a) G. E. Rudebusch, J. L. Zafra, K. Jorner, K. Fukuda, J. L. Marshall, I. Arrechea-Marcos, G. L. Espejo, R. Ponce Ortiz, C. J. Gomez-Garcia, L. N. Zakharov, M. Nakano, H. Ottosson, J. Casado, M. M. Haley, *Nat. Chem.* **2016**, *8*, 753-759; b) G. G. Dyadyusha, V. I. Lutoshkin, *Theor. Exp. Chem.* **1975**, *9*, 44-49.

[17] M. Tang, Q. Zhu, P. Hu, L. Jiang, R. Liu, J. Wang, L. Cheng, X. Zhang, W. Chen, H. Wang, *Adv. Funct. Mater.* **2021**, *31*, 2102011.

[18] a) M. Gomberg, *J. Am. Chem. Soc.* **1900**, *22*, 757–771; b) X. Ai, E. W. Evans, S. Dong, A. J. Gillett, H. Guo, Y. Chen, T. J. H. Hele, R. H. Friend, F. Li, *Nature* **2018**, *563*, 536-540.

[19] a) K. Koshika, N. Sano, K. Oyaizu, H. Nishide, *Macromol. Chem. Phys.* **2009**, *210*, 1989-1995; b) E. Schröter, L. Elbinger, M. Mignon, C. Friebe, J. C. Brendel, M. D. Hager, U. S. Schubert, *J. Power Sources* **2023**, *556*, 232293; c) K. Nakahara, S. Iwasa, M. Satoh, Y. Morioka, J. Iriyama, M. Suguro, E. Hasegawa, *Chem. Phys. Lett.* **2002**, *359*, 351-354; d) T. Ma, A. D. Easley, S. Wang, P. Flouda, J. L. Lutkenhaus, *Cell Rep. Phys. Sci.* **2021**, *2*, 100414.

[20] a) A. Badalyan, S. S. Stahl, *Nature* **2016**, *535*, 406-410; b) B. L. Ryland, S. S. Stahl, *Angew. Chem. Int. Ed.* **2014**, *53*, 8824-8838.

[21] Y. Xue, P. Guo, H.-L. Yip, Y. Li, Y. Cao, *J. Mater. Chem. A* **2017**, *5*, 3780-3785.

[22] J. Zhou, W. Zhu, M. Zeng, Q. Yang, P. Li, L. Lan, J. Peng, Y. Li, F. Huang, Y. Cao, *Sci. China: Chem.* **2019**, *62*, 1656-1665.

[23] a) Z. Chen, W. Li, Y. Zhang, Z. Wang, W. Zhu, M. Zeng, Y. Li, *J. Phys. Chem. Lett.* **2021**, *12*, 9783-9790; b) Y. Li, L. Li, Y. Wu, Y. Li, *J. Phys. Chem. C* **2017**, *121*, 8579-8588.

[24] Y. Joo, V. Agarkar, S. H. Sung, B. M. Savoie, B. W. Boudouris, *Science* **2018**, *359*, 1391-1395.

[25] X. Wang, W. Tang, K. P. Loh, *ACS Appl. Energy Mater.* **2021**, *4*, 3612-3621.

[26] P. L. Corio, S. Shih, *J. Am. Chem. Soc.* **1971**, *75*, 3475–3478.

[27] a) Y. T. Long, E. Abu-Irhayem, H. B. Kraatz, *Chem. Eur. J.* **2005**, *11*, 5186-5194; b) E. F. Yee, B. Dzikovski, B. R. Crane, *J. Am. Chem. Soc.* **2019**, *141*, 17571-17587; c) R. Tsunashima, *Acta Crystallogr., Sect. A* **2017**, *73*, C1089-C1089.

[28] a) Z. Guo, Y. Ma, X. Dong, J. Huang, Y. Wang, Y. Xia, *Angew. Chem. Int. Ed.* **2018**, *57*, 11737-11741; b) Y. Wang, C. Wang, Z. Ni, Y. Gu, B. Wang, Z. Guo, Z. Wang, D. Bin, J. Ma, Y. Wang, *Adv. Mater.* **2020**, *32*, 2000338; c) Q. Zhao, W. Huang, Z. Luo, L. Liu, Y. Lu, Y. Li, L. Li, J. Hu, H. Ma, J. Chen, *Sci. Adv.* **2018**, *4*, eaao1761.

[29] a) P. Liu, J. Qiu, X. Wu, *J. Taiwan Inst. Chem. Eng.* **2013**, *44*, 686-690; b) P. Liu, J. Qiu, X. Wu, *Mater. Lett.* **2012**, *77*, 4-6.

[30] a) Z. Lin, H. Y. Shi, L. Lin, X. Yang, W. Wu, X. Sun, *Nat. Commun.* **2021**, *12*, 4424; b) Y. Zhang, C. Zhao, Z. Li, Y. Wang, L. Yan, J. Ma, Y. Wang, *Energy Storage Mater.* **2022**, *52*, 386-394; c) H.-g. Wang, Q. Wu, L. Cheng, G. Zhu, *Coordin. Chem. Rev.* **2022**, *472*, 214772; d) L. Li, Y. Wang, W. Gong, M. Lin, L. Wei, Q. Li, Q. Zhang, L. Sun, *Chem. Eng. J.* **2023**, *465*, 142824.

[31] T. Sun, W. Zhang, Q. Nian, Z. Tao, *Chem. Eur. J.* **2023**, *452*, 139324.

Table of Contents

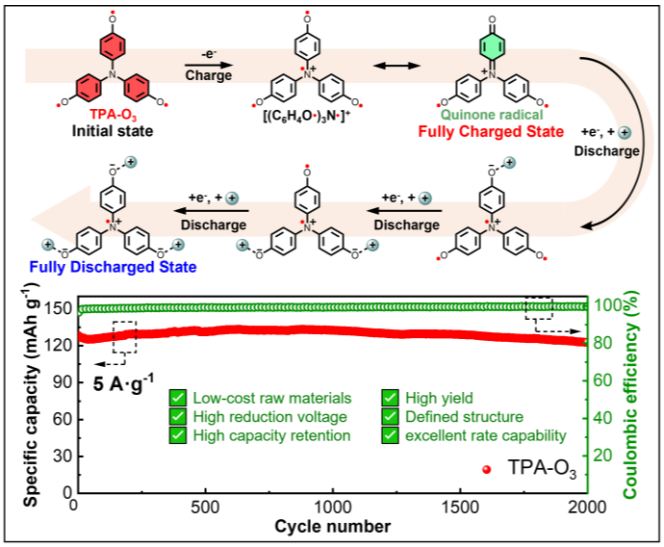

Organic radical TPA-O_3 can be synthesized through simple two steps by utilizing the extremely low-cost raw materials. Finally, the TPA-O_3 cathode shows a high-capacity retention of 95.87% after 2000 stable cycles at 5 A g^{-1}, paving the way for the cathode design of high rate and capacity battery.